V. G. Malkin, O. L. Malkina, *J. Am. Chem. Soc.* **119**, 12669 (1997).
22. An extended bibliography of NICS values is given by S. Patchkovskii and W. Thiel [*J. Mol. Model.* **6**, 67 (2000)].
23. M. J. Frisch *et al.*, Gaussian 98 (Revision A.7) (Gaussian, Pittsburgh, PA, 1998).
24. An imaginary frequency indicates the existence of a vibrational mode that is dynamically unstable and leads to a more stable structure. Transition states of a chemical reaction are saddle points exhibiting only one imaginary frequency. Saddle points with more than one imaginary frequency may be visited by dynamical systems with sufficiently high vibrational energy but are generally not of chemical significance.
25. P. v. R. Schleyer, H. Jiao, M. N. Glukhovtsev, J. Chandrasekhar, E. Kraka, *J. Am. Chem. Soc.* **116**, 10129 (1994).
26. The typical carbon-carbon, carbon-boron, and boron-boron bond lengths (B3LYP/6-311+G**) are as follows: $H_3C–CH_3$ (D_{3d}), 1.531 Å; $H_2C=CH_2$ (D_{2h}), 1.329 Å; $H_3C–BH_2$ (C_s), 1.554 Å; $CH_2=BH$ (C_{2v}), 1.376 Å; $H_2B–BH_2$ (D_{2d}), 1.629 Å; and $HB=BH$ (D_{*h}), 1.523 Å.
27. Bonding was computed at B3LYP/6-31G*//B3LYP/6-311+G*. The Natural Bond Orbital (NBO) implementation in Gaussian 98 cannot handle CB_6^{2-} at the B3LYP/6-311+G* level (linear-dependent basis set).
28. The NICS values in parts per million (*20*–*22*) (B3LYP/6-311+G**) 1.0/1.5 Å above the central carbons of **13** (−22.8/−9.7), 15 (−22.8/−10.2), **16** (−22.1/−9.9), and **17** (−23.6/−10.9) document the aromatic character of these hexacoordinate carbon species; the values above the center of benzene are −10.2/−7.6.
29. The concept of the right geometrical "fit" (*3*) is further demonstrated by species like NB_6^-, PB_6^-, OB_6, and SB_6 with a cyclic B_6 ligand. These species are isoelectronic with D_{6h} symmetrical CB_6^{2-} (**13**), but NB_6^- and SB_6 adopt D_{2h} symmetry because of a "minor" bond-length mismatch (but still feature planar hexacoordinate nitrogen and oxygen). In contrast, phosphorous and sulfur are too large to fit into the B_6 ring. Consequently, C_{6v} symmetric structures of PB_6^- and SB_6 result, having the "coordinated" atoms positioned above the B_6 plane.
30. Supplemental material is available at www.sciencemag.org/cgi/content/full/290/5498/1937/DC1.
31. Isomers **18** and **20** easily rearrange into **19** with barriers of 3.2 (**18** → **19**) and 8.9 kcal mol^{-1} (**20** → **19**), respectively.
32. T. J. Lee, P. R. Taylor, *Int. J. Quant. Chem. Quant. Chem. Symp.* **23**, 199 (1989).
33. This multireference character was also shown and taken into account by CASSCF(6,10)/6-311+G* calculations. The relative energies of **15** through **17** were reproduced well (13.3, 0.0, and 5.5 kcal mol^{-1}, respectively). Although the activation barrier for the isomerization of **15** (33.1 kcal mol^{-1}) was almost unchanged as compared to the B3LYP and CCSD(T) calculations, the barriers for **16** (8.5 kcal mol^{-1}) and **17** (12.8 kcal mol^{-1}) were smaller. CAS-MP2 runs with Gaussian 98 gave only "bizarre results," as has been noted earlier for Gaussian 94 by Th. Bally and W. T. Borden [in *Reviews in Computational Chemistry*, K. B. Lipkowitz, D. B. Boyd, Eds. (Wiley, New York, 1999), vol. 13, footnote on p. 36].
34. Generation of the hexacoordinate carbon compounds by laser vaporization of a suitable target combined with instantaneous cooling of the generated molecules to ~4 K in a supersonic jet might allow subsequent matrix isolation and/or spectroscopic detection of these exciting species, even for **16** and **17** with their lower barriers for isomerization {compare work by V. E. Bondybey, A. M. Smith, and J. Argreiter [*Chem. Rev.* **96**, 2113 (1996)] and D. S. Perry and G. A. Bethardy [in *Techniques of Chemistry Series*, A. B. Myers, Th. R. Rizzo, Eds. (Wiley, New York, 1995), vol. XXIII, chap. 3]}.
35. We thank H. Prinzbach, Freiburg, for his encouragement. This work was supported by the Fonds der Chemischen Industrie through a postdoctoral fellowship (K.E.).

19 June 2000; accepted 1 November 2000

REPORTS

Geodynamic Evidence for a Chemically Depleted Continental Tectosphere

Alessandro M. Forte* and H. K. Claire Perry

The tectosphere, namely the portions of Earth's mantle lying below cratons, has a thermochemical structure that differs from average suboceanic mantle. The tectosphere is thought to be depleted in its basaltic components and to have an intrinsic buoyancy that balances the mass increase associated with its colder temperature relative to suboceanic mantle. Inversions of a large set of geodynamic data related to mantle convection, using tomography-based mantle flow models, indicate that the tectosphere is chemically depleted and relatively cold to 250 kilometers depth below Earth's surface. The approximate equilibrium between thermal and chemical buoyancy contributes to cratonic stability over geological time.

The tectosphere refers to the mantle below continental lithosphere that is assumed to be stabilized against convective disruption by a balance between thermally generated negative buoyancy and positive chemical buoyancy (*1*, *2*). Seismic, petrologic, and heat flow data have suggested that both the subcontinental chemical boundary layer (CBL) and thermal boundary layer (TBL) extend to about 200 km depth (*3*, *4*). More recent studies based on continental heat flow and gravity data indicate that the tectosphere TBL extends to depths between 200 and 330 km (*5*, *6*). Additional constraints on the thermochemical structure and depth extent of the tectosphere are provided by mantle xenolith data (*7*–*9*). The interpretation of heat flow and gravity data is, however, nonunique, and the xenolith data represent a limited sampling of the deep structure of the tectosphere.

High-resolution seismic tomography provides detailed reconstructions of the three-dimensional (3D) structure in the mantle (*10*–*13*). Tomographic models derived from short-period seismic surface waves (*10*, *13*) provide optimal vertical resolution of the 3D structure in the tectosphere (*14*). These 3D models show a tectosphere characterized by sublithospheric shear wave speeds about 5% faster than shear wave speeds in the ambient mantle. A recent interpretation of this shear velocity heterogeneity suggests that the tectosphere TBL extends to a maximum depth of about 230 km, but a corresponding CBL was not detected (*15*). Shear velocity anomalies alone cannot distinguish chemical heterogeneity in the tectosphere, unless they are combined with constraints on the tectosphere density structure (*16*).

We derived constraints on the tectosphere density structure using a reformulated mantle flow theory (*17*) that incorporates surface tectonic plates whose motions are coupled to the underlying mantle flow. In the flow modeling, we used two recent high-resolution models of seismic shear wave velocity heterogeneity (*11*, *13*), which are derived from independent data, using different parameterizations of the heterogeneity and different inversion procedures. Constraints on mantle density anomalies, and consequently the thermochemical structure of the tectosphere, are then obtained by inverting convection-related geodynamic data with the mantle flow model.

The convection data we use are the tectonic plate velocities (*18*), the global free-air gravity anomalies (*19*), the surface topography corrected for crustal isostasy (*20*), and the excess or dynamic ellipticity of the core-mantle boundary (*21*, *22*). These data provide independent constraints on mantle density, with different sensitivities to density anomalies at different depths (*23*). The surface topography (Fig. 1) provides the strongest constraint on density variations in the lithospheric mantle, and thus a number of tomography-based mantle flow studies have used surface topography to constrain the density structure and dynamics of the tectosphere (*24*–*27*).

We first estimated mantle density anomalies ($\delta\rho$), which provide the buoyancy forces for mantle flow, from shear wave velocity anomalies (δV_s) using a mineral physics estimate (*28*) of the velocity-to-density conversion $d\ln\rho/d\ln V_s$. Mantle flow modeling also requires a knowledge of mantle rheology, which we represent as a depth-dependent viscosity. We derived the mantle viscosity profile through nonlinear iterative inversions (*17*) of the convection data, using the initial estimate of $\delta\rho$. The viscosity profiles we obtained (Fig. 2A) are characterized by a low-viscosity zone at ~200 km depth.

The density structure of the tectosphere is

Department of Earth Sciences, University of Western Ontario, London, Ontario N6A 5B7, Canada.

*To whom correspondence should be addressed. E-mail: aforte@uwo.ca

determined by inverting the convection data for a given tomographic model and viscosity profile. We isolated the shear wave velocity heterogeneity associated with the tectosphere, so that its density could be inferred independently of the rest of the upper mantle, by identifying those portions of the mantle lying below cratons. We thus delineated the depth-dependent horizontal extent of the tectosphere and the corresponding shear wave velocity anomalies, which we denote by $(\delta V_s/V_s)_{sh}$, where sh stands for shield. The seismic anomalies exterior to the tectosphere are denoted by $(\delta V_s/V_s)_{th}$, where th stands for thermal on the expectation that the seismic anomalies outside the tectosphere are primarily thermal in origin. This last assumption may not be accurate in tectonically active regions characterized by substantial basaltic magmatism.

We inverted the convection data to infer the velocity-density scaling coefficient for shield and thermal mantle, $(d\ln\rho/d\ln V_s)_{sh}$ and $(d\ln\rho/d\ln V_s)_{th}$, respectively. If V_s anomalies were due only to temperature differences, then $(d\ln\rho/d\ln V_s)_{sh} = (d\ln\rho/d\ln V_s)_{th}$. The effect of lower seismic attenuation in the tectosphere due to colder temperatures (*3*) would imply $(d\ln\rho/d\ln V_s)_{sh} > (d\ln\rho/d\ln V_s)_{th}$ (*28*). We instead find (Fig. 2B) that $(d\ln\rho/d\ln V_s)_{sh} < (d\ln\rho/d\ln V_s)_{th}$, implying that the density anomalies in the tectosphere may not be caused solely by temperature variations and suggesting the presence of chemical heterogeneity. The relative density perturbations in the tectosphere, $(\delta\rho/\rho)_{sh} = (d\ln\rho/d\ln V_s)_{sh}(\delta V_s/V_s)_{sh}$, show a peak amplitude at ~130 km depth, with negligible amplitude below 250 km (dashed lines, Fig. 2C). The agreement between predicted and observed dynamic topography (Fig. 1) obtained on the basis of the velocity-density conversion factors is comparable to the fit to other geodynamic data (Table 1).

We considered two estimates of chemical heterogeneity, one based on internal consistency of our $d\ln\rho/d\ln V_s$ inferences and the other based on independent mineral physics constraints (*29*). The chemical heterogeneity inferred on the basis of either approach suggests greater iron and garnet depletion in the top portion of the tectosphere, with a maximum depletion at about 130 km depth (Fig. 3). The inferred chemical heterogeneity diminishes rapidly below 250 km depth, suggesting a demarcation for the base of the CBL at this depth. The maximum inferred iron depletion, $\delta R = -0.024$ at 130 km depth (Fig. 3), suggests as much as 20% fractionation of basalt in the tectosphere [see Table 6

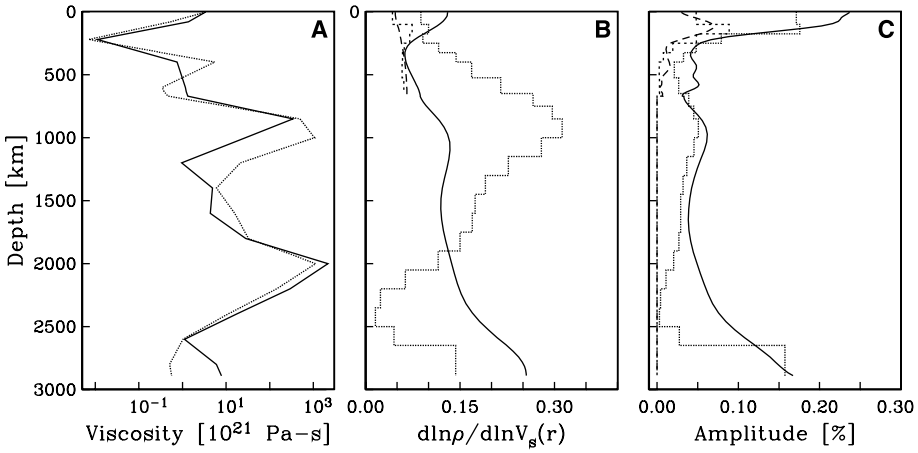

Fig. 2. Mantle viscosity and density structure. (**A**) The depth-dependent effective viscosity of the mantle obtained through inversions of geodynamic data (Table 1) with the tomography models of Grand *et al.* (*11*) (dotted curve) and Ekström and Dziewonski (*13*) (solid curve). For these inversions, the mantle density anomalies were derived from the seismic anomalies with a mineral physics estimate (*28*) of $d\ln\rho/d\ln V_s$. (**B**) Velocity-density scaling, $d\ln\rho/d\ln V_s$, obtained through inversions of the geodynamic data (Table 1). The long- and short-dashed curves represent the scaling $(d\ln\rho/d\ln V_s)_{sh}$ inferred for tectosphere seismic anomalies in the models of Ekström and Dziewonski and Grand *et al.*, respectively. The solid and dotted curves represent the scaling $(d\ln\rho/d\ln V_s)_{th}$ inferred for the seismic anomalies outside the tectosphere in the models of Ekström and Dziewonski and Grand *et al.*, respectively. (**C**) The root-mean-square (rms) amplitude of density anomalies. The solid and dotted curves represent the rms amplitude of density anomalies $(\delta\rho/\rho)_{th}$ (*29*) outside the tectosphere in the models of Ekström and Dziewonski and Grand *et al.*, respectively. The long- and short-dashed curves represent the rms amplitude of tectosphere density anomalies $(\delta\rho/\rho)_{sh}$ (*29*) derived from the models of Ekström and Dziewonski and Grand *et al.*, respectively.

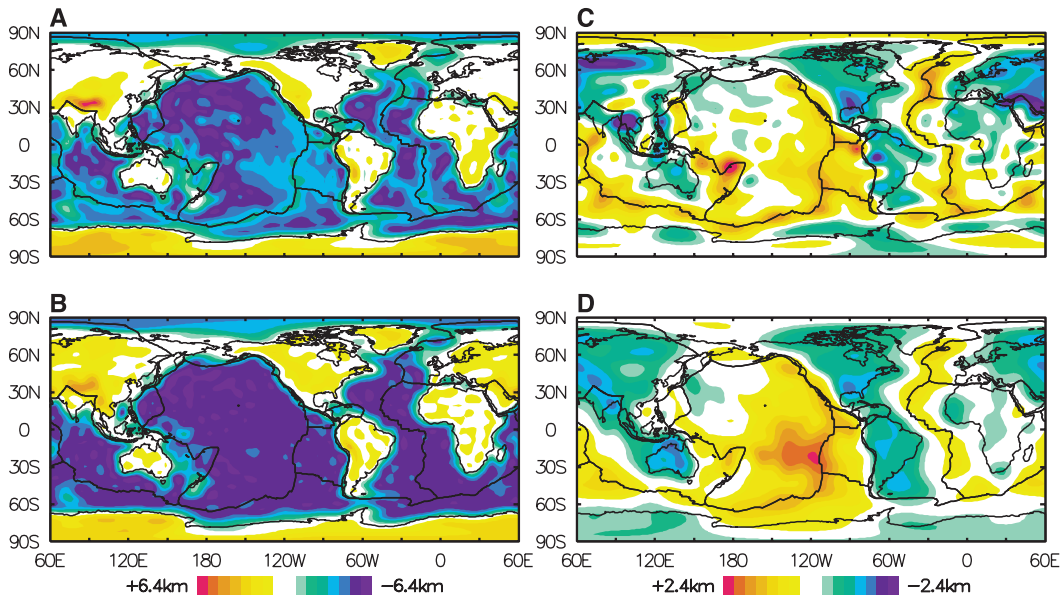

Fig. 1. Global isostatic and dynamic topography. (**A**) Observed surface topography (from the ETOPO5 compilation) represented by a spherical harmonic expansion in the degree range $l = 0$ to 32. (**B**) Isostatic surface topography, calculated on the basis of a recent compilation (*20*) of crustal thickness and density, represented by spherical harmonics in the degree range $l = 0$ to 32. A model of Airy isostasy [for example, (*24*, *26*)] is assumed in this calculation. (**C**) The residual or dynamic topography, in the degree range $l = 1$ to 20, obtained by subtracting the isostatic topography in (B) from that observed in (A). (**D**) The dynamic surface topography, in the degree range $l = 1$ to 20, predicted on the basis of the mantle viscosity and density structure (Fig. 2, A and C) inferred on the basis of the Ekström and Dziewonski (*13*) tomography model.

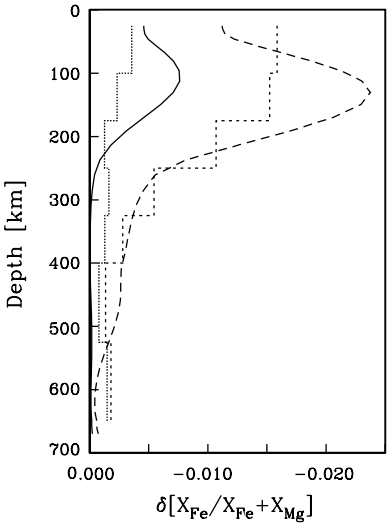

Fig. 3. Iron depletion δR (*16*) in the tectosphere. The dotted and solid curves represent the internally consistent estimate (*29*) of tectosphere chemical heterogeneity, expressed in terms of peak values of the perturbation to the iron ratio R, inferred from the models of Grand *et al.* (*11*) and Ekström and Dziewonski (*13*), respectively. The long- and short-dashed curves represent the estimate of δR, obtained with independent mineral physics data (*28*), inferred from the models of Ekström and Dziewonski and Grand *et al.*, respectively. The latter estimate provides better agreement between the inferences obtained from the two tomography models.

Table 1. Fits to global convection data. All fits, with the exception of the core-mantle boundary (CMB) topography, are expressed in terms of variance reduction.

3D mantle model*	Free-air gravity† [l = 2 to 20]	Plate divergence‡ [l = 1 to 32]	Surface topography§ [l = 1 to 20]	Excess CMB ellipticity‖
Ek&Dz¶	37% (77%)	57%	−64%	−0.16 km
Grand¶	31% (62%)	61%	22%	0.50 km
Ek&Dz#	36% (63%)	64%	48%	0.52 km
Grand#	32% (65%)	60%	41%	0.52 km

*Mantle flow predictions of geodynamic observables use two tomographic models: "Ek&Dz" (*13*) and "Grand" (*11*). †The observed free-air gravity anomalies are calculated with the nonhydrostatic gravitational potential derived from satellite data (*19*). The numbers in parentheses are the variance reductions to the equivalent geoid anomalies (variations in height of the gravitational equipotential surface) derived from satellite data. The wavelength-dependent amplitude spectra of the geoid and gravity anomalies are quite different, with the latter having a relatively flat spectrum, which explains why the fits to the anomalous gravity and geoid fields differ. ‡The plate motion data are represented here in terms of the horizontal divergence of the plate velocities given by the NUVEL-1 model (*18*). §The dynamic surface topography is obtained from observed surface topography after removal of the crustal isostatic contribution (Fig. 1). ‖ The most recent inference (*22*) of excess or dynamic CMB ellipticity suggests a value of about 0.4 km, rather than 0.5 km as determined in earlier studies (*21*). ¶The density perturbations in the mantle flow models are derived from the shear velocity anomalies with $d\ln\rho/d\ln V_s$ obtained by Karato (*28*). #The density perturbations are derived on the basis of the associated $d\ln\rho/d\ln V_s$ profiles (Fig. 2B) inferred in inversions of the convection data.

in (*7*)]. The spatial distribution of chemical anomalies and corresponding thermal anomalies (Fig. 4) shows zones of maximum depletion and coldest temperatures lying directly below the Precambrian cratons.

We determined depth-dependent temperature anomalies (geotherm perturbations) at a number of sites (Fig. 4C). All geotherms (Fig. 5A) display maximum temperature perturbations between 100 and 150 km depth and then decrease to low values below 250 km depth as the geotherms approach the average adiabatic mantle geotherm. We examined the plausibility of these temperature inferences through an independent calculation of average upper-mantle and subcontinental geotherms (Fig. 5B), using surface heat flow observations (*30*). The difference between the subcontinental and average mantle geotherms (dashed line, Fig. 5A) is consistent with the perturbed geotherms inferred from the tomographic model. The ~50-km vertical shift between the two sets of geotherms is probably not significant, considering the radial smoothing and imperfect radial resolution (*14*) in the tomographic model.

The magnitude and depth extent of the chemical anomalies in the tectosphere depend on the density anomalies inferred from the geodynamic data, through the $d\ln\rho/d\ln V_s$ profiles (*29*). Because the geodynamic data depend only on mantle density structure, irrespective of its thermal or chemical origin, they constrain the tectosphere heterogeneity independently of constraints provided by seismic data. Our combined geodynamic and seismic interpretation of tectosphere structure suggests that the location of the base of the TBL (Fig. 5) matches the base of the CBL (Fig. 3), consistent with the hypothesis (*3*) that thermal buoyancy is stabilized by chemical buoyancy. We find that the tectosphere buoyancy ratio R_ρ, which measures the relative importance of chemical and thermal

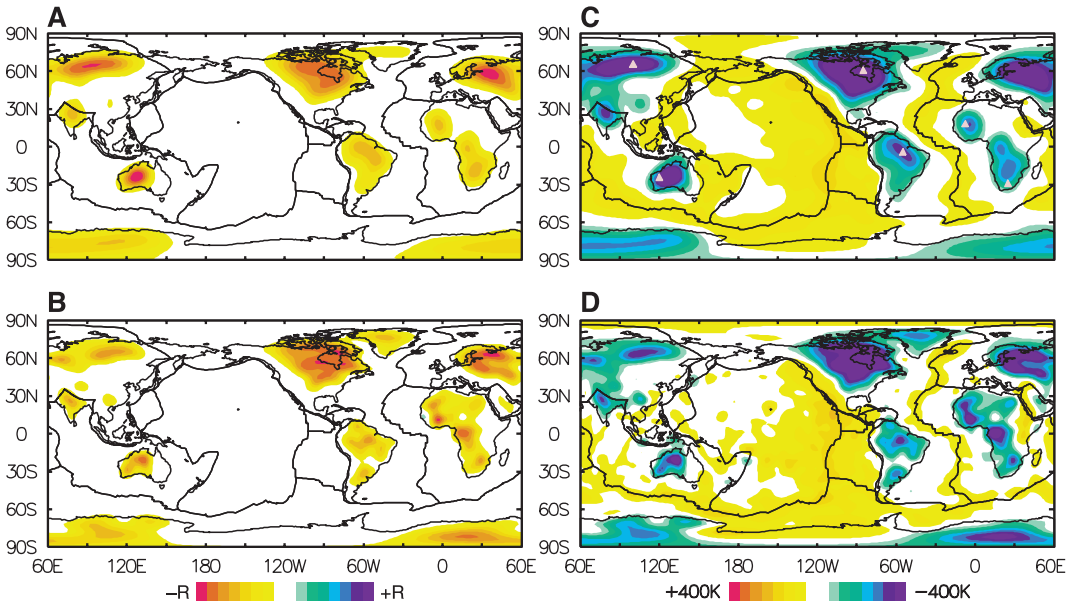

Fig. 4. Chemical and thermal structure of the mantle at 150 km depth. (**A**) Iron depletion δR (*16*) in the tectosphere inferred on the basis of the Ekström and Dziewonski model (*13*) and using independent mineral physics data to estimate the thermal properties of the tectosphere (*28*). The heterogeneity shown here is represented by spherical harmonics in the degree range l = 0 to 20. Scale limit R = 2.0%. (**B**) Iron depletion δR, in the degree range l = 0 to 32, obtained as in (A) but with Grand *et al.*'s model (*11*). (**C**) Lateral temperature variations, in the degree range l = 1 to 20, inferred on the basis of the Ekström and Dziewonski model and using, as in (A), independent mineral physics constraints on the tectosphere's thermal properties. The small light gray triangles identify locations that are sampled to study the vertical temperature profile in the tectosphere (see Fig. 5A). (**D**) Lateral temperature variations, in the degree range l = 1 to 32, obtained as in (C) but with Grand *et al.*'s model. Scale limit R = 1.6%.

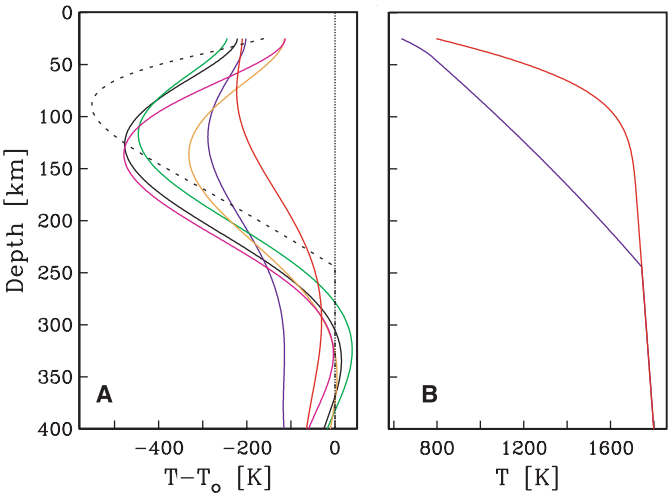

Fig. 5. Temperature profiles (geotherms) in the tectosphere. (**A**) The depth variation of the (negative) temperature perturbations estimated, as in Fig. 4C, from the Ekström and Dziewonski model (*13*). Each colored curve corresponds to a geographic location identified by small light gray triangles in Fig. 4C: Hudson Bay (black), central Brazil (orange), west Africa (blue), south Africa (red), Siberia (violet), and west Australia (green). The dashed black line represents a theoretical estimate obtained by differencing the two reference geotherms in (**B**), where the blue and red curves represent an average temperature profile below continental shields and a globally averaged temperature profile, respectively (*30*).

buoyancy (*29*), is ~0.8, consistent with numerical models showing that the tectosphere is stably supported over billion year time scales (*31*).

References and Notes

1. T. H. Jordan, *Rev. Geophys.* **13**, 1 (1975).
2. _____, *Nature* **274**, 544 (1978).
3. _____, *Philos. Trans. R. Soc. London Ser. A* **301**, 359 (1981).
4. D. L. Anderson, *J. Geophys. Res.* **92**, 13968 (1987).
5. C. Jaupart, J.-C. Mareschal, *Lithos* **48**, 93 (1999).
6. M.-P. Doin, L. Fleitout, D. McKenzie, *J. Geophys. Res.* **101**, 16119 (1996).
7. T. H. Jordan, in *The Mantle Sample: Inclusions in Kimberlites and Other Volcanics*, F. R. Boyd, H. O. A. Meyer, Eds. (American Geophysical Union, Washington, DC, 1979), pp. 1–14.
8. A. A. Finnerty, F. R. Boyd, in *Mantle Xenoliths*, P. H. Nixon, Ed. (Wiley, New York, 1987), pp. 381–402.
9. R. L. Rudnick, W. F. McDonough, R. J. O'Connell, *Chem. Geol.* **145**, 395 (1998).
10. J. H. Woodhouse, J. Trampert, *Eos* (Fall Meet. Suppl.), **76**, 422 (1995).
11. S. P. Grand, R. D. van der Hilst, S. Widiyantoro, *GSA Today* **7**, 1 (1997).
12. H. Bijwaard, W. Spakman, E. R. Engdahl, *J. Geophys. Res.* **103**, 30055 (1998).
13. G. Ekström, A. M. Dziewonski, *Nature* **394**, 168 (1998).
14. The previous generation of global tomography models [for example, W.-J. Su, R. L. Woodward, A. M. Dziewonski, *J. Geophys. Res.* **99**, 6945 (1994)] was characterized by a maximum horizontal resolution corresponding to spherical harmonic degree 8 or 12 (equivalent to a minimum horizontal half-wavelength of 2400 or 1600 km, respectively, at the surface). These models also had a theoretical depth resolution of about 100 km (assuming a Chebyshev polynomial expansion to order 13). In contrast, the tomographic model of Ekström and Dziewonski (*13*) has a horizontal resolution scale of about 1000 km and a vertical resolution scale, in the upper mantle, of about 50 km.
15. A. H. E. Röhm, R. Snieder, S. Goes, J. Trampert, *Earth Planet. Sci. Lett.* **181**, 395 (2000).
16. The combined effects of lateral variations in temperature and composition on variations in seismic shear wave velocity ($\delta V_s/V_s$) and density ($\delta\rho/\rho$) in the tectosphere may be expressed by

$$\frac{\delta\rho}{\rho} = -\alpha\delta T + \frac{\partial \ln \rho}{\partial R}\delta R + \frac{\partial \ln \rho}{\partial X_{Gt}}\delta X_{Gt}$$

$$\frac{\delta V_s}{V_s} = \frac{\partial \ln V_s}{\partial T}\delta T + \frac{\partial \ln V_s}{\partial R}\delta R + \frac{\partial \ln V_s}{\partial X_{Gt}}\delta X_{Gt}$$

where δT are the temperature perturbations and, following Jordan (*7*), the compositional heterogeneity is expressed in terms of the iron molar ratio $R = X_{Fe}/(X_{Fe} + X_{Mg})$ and the molar fraction of garnet in the whole rock, X_{Gt}. Using the estimates (*7*)

$$\frac{\partial \ln V_s}{\partial R} = -0.34, \quad \frac{\partial \ln V_s}{\partial X_{Gt}} = +0.05$$

$$\frac{\partial \ln \rho}{\partial R} = +0.32, \quad \frac{\partial \ln \rho}{\partial X_{Gt}} = +0.10$$

and assuming 10% fractionation of basalt from fertile subcontinental lherzolite, for which $\delta R \simeq -0.013$ and $\delta X_{Gt} \simeq -0.056$ [see Table 6 in (*7*)], yield the following compositional perturbations:

$$\frac{\delta V_s}{V_s} = +0.16\%, \quad \frac{\delta\rho}{\rho} = -0.98\%$$

Assuming a temperature perturbation of −500°, at about 100 km depth (*5*), yields the following thermal perturbations:

$$\frac{\delta V_s}{V_s} = -7.0\%, \quad \frac{\delta\rho}{\rho} = +1.75\%$$

where we have assumed $\alpha = 3.5 \times 10^{-5}$ K^{-1} and $\partial \ln V_s/\partial T = -14 \times 10^{-5}$ K^{-1} (*28*). On the basis of these estimates, the compositional heterogeneity due to basalt depletion in the tectosphere will have a negligible effect on V_s (*15*), whereas the effect on ρ will be large, producing changes in excess of 50%.
17. A. M. Forte, in *Earth's Deep Interior: Mineral Physics and Tomography from the Atomic to the Global Scale*, S.-i. Karato *et al.*, Eds., vol. 117 of *Geophysical Monograph Series* (American Geophysical Union, Washington, DC, 2000), pp. 3–36.
18. C. R. De Mets, R. G. Gordon, D. F. Argus, S. Stein, *Geophys. J. Int.* **101**, 425 (1990).
19. J. G. Marsh *et al.*, *J. Geophys. Res.* **95**, 22043 (1990).
20. W. D. Mooney, G. Laske, T. G. Masters, *J. Geophys. Res.* **103**, 727 (1998).
21. C. R. Gwinn, T. A. Herring, I. I. Shapiro, *J. Geophys. Res.* **91**, 4755 (1986).
22. P. Mathews, B. A. Buffet, T. A. Herring, *Eos* (Fall Meet. Suppl.) **80** (no. 46), 19 (1999).
23. The theoretical sensitivity of the convection-related data to mantle density anomalies is characterized in terms of mathematical kernel functions that represent the dynamic response of the viscous mantle to density loads placed at different depths. These sensitivities also depend on the depth variation of the effective viscosity of the mantle. An extensive discussion of the basic mantle flow theory and the geodynamic kernel functions is provided by B. H. Hager and R. W. Clayton [in *Mantle Convection: Plate Tectonics and Global Dynamics*, W. R. Peltier, Ed. (Gordon & Breach, New York, 1989), pp. 657–763].
24. A. M. Forte, W. R. Peltier, A. M. Dziewonski, R. L. Woodward, *Geophys. Res. Lett.* **20**, 225 (1993).
25. A. M. Forte, A. M. Dziewonski, R. J. O'Connell, *Phys. Earth Planet. Inter.* **92**, 45 (1995).
26. G. Pari, W. R. Peltier, *J. Geophys. Res.* **105**, 5635 (2000).
27. One difficulty in the previous mantle flow modeling of dynamic topography in continental regions (*24–26*) was the viscous flow theory itself. One of the key factors governing flow dynamics in the mantle, especially in the upper mantle, is the nature of the surface boundary condition. The previously cited mantle flow studies all assumed a free-slip surface boundary, in effect ignoring the presence of rigid tectonic plates at the surface. As recently shown by Forte [Fig. 9 in (*17*)], the plates suppress the shallow subcontinental flow more strongly than in the case of a free-slip surface. The buoyancy-induced flow below continents and away from plate boundaries sees an effectively no-slip surface. The kernel functions (*23*) for surface topography are also affected by the assumed surface boundary condition: For a free-slip surface, the kernel amplitudes in the upper mantle are smaller than the amplitudes obtained for a no-slip surface. This amplitude difference is greatest for the very long horizontal wavelength density anomalies used in the previous modeling of dynamic topography. In other words, for a given density structure and viscosity profile, mantle flow models of dynamic surface topography that assume a free-slip surface underestimate the amplitude of the topography in continental regions and thereby yield a biased constraint on density anomalies in the tectosphere.
28. S.-i. Karato, *Geophys. Res. Lett.* **20**, 1623 (1993).
29. If we assume that perturbations in iron and garnet content are correlated in the tectosphere, owing to simultaneous variations in both as a result of basalt depletion (*7*), then on the basis of the expressions in (*16*) we obtain

$$\left(\frac{\delta\rho}{\rho}\right)_{sh} = -\alpha\delta T + A\delta R = \left(\frac{d \ln \rho}{d \ln V_s}\right)_{sh}\left(\frac{\delta V_s}{V_s}\right)_{sh}$$

$$\left(\frac{\delta V_s}{V_s}\right)_{sh} = -\alpha\left(\frac{\partial \ln V_s}{\partial \ln \rho}\right)_{th}\delta T + B\delta R$$

where

$$A = \frac{\partial \ln \rho}{\partial R} + \frac{\partial \ln \rho}{\partial X_{Gt}}\frac{\delta X_{Gt}}{\delta R}$$

$$B = \frac{\partial \ln V_s}{\partial R} + \frac{\partial \ln V_s}{\partial X_{Gt}}\frac{\delta X_{Gt}}{\delta R}$$

Solving for δT and δR yields

$$\delta T = -\frac{1}{\alpha}\left(\frac{d \ln \rho}{d \ln V_s}\right)_{sh}\left[\left(\frac{d \ln V_s}{d \ln \rho}\right)_{sh} - \frac{B}{A}\right]$$
$$\left[\left(\frac{\partial \ln V_s}{\partial \ln \rho}\right)_{th} - \frac{B}{A}\right]^{-1}\left(\frac{\delta V_s}{V_s}\right)_{sh}$$

$$\delta R = \frac{1}{A}\left[\left(\frac{\partial \ln V_s}{\partial \ln \rho}\right)_{th}\left(\frac{d \ln \rho}{d \ln V_s}\right)_{sh} - 1\right]$$
$$\left[\left(\frac{\partial \ln V_s}{\partial \ln \rho}\right)_{th} - \frac{B}{A}\right]^{-1}\left(\frac{\delta V_s}{V_s}\right)_{sh}$$

In the "thermal" mantle, outside the tectosphere, where compositional heterogeneity is assumed to be negligible, we have

$$\left(\frac{\delta\rho}{\rho}\right)_{th} = -\alpha\delta T = \left(\frac{d \ln \rho}{d \ln V_s}\right)_{th}\left(\frac{\delta V_s}{V_s}\right)_{th} \Rightarrow$$

$$\delta T = -\frac{1}{\alpha}\left(\frac{d \ln \rho}{d \ln V_s}\right)_{th}\left(\frac{\delta V_s}{V_s}\right)_{th}$$

The buoyancy ratio R_ρ describes the relative importance of density anomalies produced by chemical and thermal effects, $(\delta\rho)_{ch}$ and $(\delta\rho)_{th}$, respectively. From the above expressions, we obtain

$$R_\rho = \frac{(\delta\rho)_{ch}}{(\delta\rho)_{th}} = \frac{A\delta R}{-\alpha\delta T} = \left[\left(\frac{\partial \ln V_s}{\partial \ln \rho}\right)_{th}\left(\frac{d \ln \rho}{d \ln V_s}\right)_{sh} - 1\right]$$

$$\times \left(\frac{d\ln\rho}{d\ln V_s}\right)_{sh}^{-1}\left[\left(\frac{d\ln V_s}{d\ln\rho}\right)_{sh} - \frac{B}{A}\right]^{-1}$$

When calculating temperature and chemical anomalies inside the tectosphere, we use estimates for $(\partial\ln V_s/\partial\ln\rho)_{th}$ to determine effects of temperature variations on V_s. One possibility is to use the velocity-density scaling $(d\ln\rho/d\ln V_s)_{th}$ inferred for the thermal mantle. This approach is internally consistent because it relies entirely on geodynamic constraints. One potential weakness with this approach is the possible presence of partial melting, or thermally induced V_s attenuation in the thermal mantle, making the application of the geodynamically inferred $(d\ln\rho/d\ln V_s)_{th}$ inappropriate in the context of the tectosphere. This leads us to consider an alternative approach in which we use independent mineral physics estimates for $(\partial\ln V_s/\partial\ln\rho)_{th}$. For this purpose, we used an average value of $(\partial\ln V_s/\partial\ln\rho)_{th} \approx 4$ in the upper mantle (*28*). In both approaches, we used the estimate $\delta X_{Gt}/\delta R \sim 4$ [see Fig. 1 in (*7*)] to determine the quantities *A* and *B* defined above. We also assumed a thermal expansion coefficient that varies linearly from $\alpha = 3.3 \times 10^{-5}$ K^{-1} at the top of the mantle to $\alpha = 2.5 \times 10^{-5}$ K^{-1} at the bottom of the upper mantle.

30. We modeled the subcontinental geotherm assuming a steady-state, conductive temperature variation that satisfies a given surface heat flow and also includes distributed radioactive heat sources in the continental crust and in the subcontinental mantle [(*32*), pp. 145–148]. The geotherm was constrained to satisfy an average continental heat flow of 48 mW/m^2, an average crustal thickness of 41 km, an average crustal heat production of 0.77 μW/m^3, and an average mantle heat production of 0.02 μW/m^3 (*9*). These parameters yield a mantle heat flux of 16 mW/m^2 at the base of the continental crust, consistent with previously proposed values (*5*). The average mantle geotherm was modeled with a cooling half-space model [(*32*), pp. 163–167] that was constrained to satisfy a globally averaged mantle heat flow of 65 mW/m^2 (from the weighted average of 16 mW/m^2 in continental regions and 97 mW/m^2 in oceanic regions) and was also constrained to join an average mantle adiabat (with average gradient of 0.36 K/km) that was pinned to a temperature of 1800 K at 400 km depth, corresponding to the phase transition of forsterite to β-Mg_2SiO_4 [A. Chopelas, *J. Geophys. Res.* **96**, 11817 (1991)].
31. S. S. Shapiro, B. H. Hager, T. H. Jordan, *Lithos* **48**, 115 (1999).
32. D. L. Turcotte, G. Schubert, *Geodynamics* (Wiley, New York, 1982).

33. We thank the referees for constructive, useful comments. We also thank the Canadian Natural Sciences and Engineering Research Council and Project LITHOPROBE for their support.

21 September 2000; accepted 10 November 2000

Teleconvection: Remotely Driven Thermal Convection in Rotating Stratified Spherical Layers

Keke Zhang* and Gerald Schubert†

We report the discovery of a convective phenomenon found to occur in a rotating spherical system in which an inner convectively unstable fluid layer is bounded by a corotating outer convectively stable fluid layer. Although convection is thermally driven in the unstable interior, the resulting convective motions concentrate primarily in the stable outer region. This phenomenon, which we term teleconvection, suggests that fluid motions observed at the "surface" of a planet (such as Jupiter's alternating zonal winds) may be driven by an energy source located deep inside the planet.

In many geophysical and astrophysical systems there exist rapid changes in the nature and strength of radial density stratification. Often, a convectively unstable deep interior is surrounded by an outer stably stratified layer (*1*). Convective fluid motions taking place in an unstable fluid may penetrate partially into a neighboring stably stratified region, a phenomenon termed penetrative convection (*2*). The problem of penetrative convection has been extensively studied in various systems [e.g., (*3*); for a review, see (*4*)]. Most studies of penetrative convection have used a nonrotating, plane-layer geometry that cannot capture all the physics of rotating spherical convection. The dynamics of thermal convection in rapidly rotating spherical systems, in which fluid motions are affected by the Coriolis force and spherical geometry, is fundamentally different from that in nonrotating, plane-layer systems (*5–10*). Although penetration into the stable region in a nonrotating convection is weak and spatially restricted (*2, 3*), it can penetrate deeper in a rotating, spherical geometry (*11*).

Planetary and astrophysical convection are usually influenced by spherical geometry, rotation, and the presence of stably stratified layers. Hence, we consider a two-layer convection system: a spherical convectively unstable fluid layer in the region $r_i \le r \le r_m$ characterized by a superadiabatic radial temperature gradient $\partial\Theta_o(r)/\partial r = -|\beta|$, and a spherical convectively stable layer in the region $r_m \le r \le r_o$ characterized by a subadiabatic radial temperature gradient $\partial\Theta_o(r)/\partial r = \delta|\beta|$, where (r, θ, ϕ) are spherical polar coordinates with $r = 0$ at the center of the sphere, Θ_o is the basic temperature field, β is a constant, r_i is the inner radius of the spherical fluid layer, r_m is the interface between the stable and unstable layers, and r_o is the outer radius of the spherical fluid layer. Parameter δ provides a measure of the strength of stable stratification in the outer spherical layer. The whole spherical system rotates uniformly with angular velocity Ω. If $\delta = -1$, the problem is identical to the well-studied convection problem (*12*). When $\delta = 1$, the superadiabatic gradient in the unstable layer has the same amplitude as the subadiabatic gradient in the stable layer. The convection model, apart from spherical geometry and rotation, is essentially the same as penetrative convection models previously studied in plane-layer geometry (*4*). We chose $r_i = r_o/3$ and $r_m = 2r_o/3$ for the purpose of illustration. We also assume that the Boussinesq approximation is valid and the amplitude of convection is so small (the dimensionless velocity **u** measured on the viscous time scale is $|\mathbf{u}| \ll 1$) that nonlinear effects can be neglected. It is unlikely that moderate nonlinear effects with $|\mathbf{u}| = O(1)$ (i.e., on the order of 1) would change the key properties of convection in a rapidly rotating spherical system because the effect of rotation is always controlling and dominant (*13*).

In addition to the stratification parameter δ, there are three nondimensional parameters in this convection problem: the Prandtl number *Pr*, the Taylor number *Ta*, and the Rayleigh number *R*, defined as

$$Pr = \frac{\nu}{\kappa} \quad (1)$$

$$Ta = \frac{4\Omega^2(r_o - r_i)^4}{\nu^2} \quad (2)$$

$$R = \frac{g\alpha|\beta|(r_o - r_i)^4}{\nu\kappa} \quad (3)$$

where *g* is the averaged radial acceleration due to gravity, ν is the kinematic viscosity of the fluid, κ is its thermal diffusivity, and α is its coefficient of thermal expansion; ν, κ, and α are assumed constant and the same in the stable and unstable regions. *Pr* measures the relative efficiency of viscous and thermal diffusion, *Ta* provides a dimensionless measure of the rotation rate, and *R* measures the strength of buoyancy forces in the deep unstable spherical layer $r_i \le r \le r_m$. For planetary atmospheres, *Ta* is usually large ($\gg 1$), whereas *Pr* may be small ($\ll 1$), especially

Department of Earth and Space Sciences and Institute of Geophysics and Planetary Physics, University of California, Los Angeles, CA 90095, USA.

*Present address: School of Mathematical Sciences, University of Exeter, Exeter EX4 4QE, UK.
†To whom correspondence should be addressed.